Article:
Stackhouse, S, Stixrude, L and Karki, BB (2015) First-principles calculations of the lattice thermal conductivity of the lower mantle. Earth and Planetary Science Letters, 427. 11 - 17. ISSN 0012-821X

https://doi.org/10.1016/j.epsl.2015.06.050

First-principles calculations of the lattice thermal conductivity of the lower mantle - Supplementary Material

Stephen Stackhouse[a,*], Lars Stixrude[b], Bijaya, B. Karki[c]

[a] *School of Earth and Environment, University of Leeds, Leeds LS2 9JT, United Kingdom.*

[b] *Department of Earth Sciences, University College London, Gower Street, London WC1E 6BT, United Kingdom.*

[c] *School of Electrical Engineering and Computer Science, Department of Geology and Geophysics, and Center for Computation and Technology, Louisiana State University, Baton Rouge, LA70803, United States of America.*

**E-mail addresses: s.stackhouse@leeds.ac.uk; l.stixrude@ucl.ac.uk; karki@csc.lsu.edu*

S1 Lattice Thermal Conductivity Model

In order to derive additional physical insight into our results and relate them to experiments at lower temperatures and pressures, we develop a simple model of the variation of lattice thermal conductivity with density and temperature

$$k(\Omega,T) = Ak_{LS} f\left(\frac{T}{BT_S}\right) C \tag{S1}$$

where $k(\Omega,T)$ is the lattice thermal conductivity at the mean atomic volume Ω and temperature T,

$$k_{LS} = \frac{\sqrt{2}}{6\pi^3\left(6\pi^2\right)^{2/3}}\left(\frac{k_B}{\hbar}\right)^3 \frac{M\Omega^{1/3}\theta^3}{\gamma^2 T} \tag{S2}$$

is the Liebfried-Schlömann relation, with M the mean atomic mass, θ the Debye temperature, γ the Grüneisen parameter, k_B the Boltzmann constant, and $\hbar$ the Planck constant divided by 2π (Roufosse and Klemens, 1974). Since different derivations yield different values for the numerical pre-factor, but equivalent functional dependencies of the physical properties, we retain the coefficient A as a parameter of order unity to be determined (Roufosse and Klemens, 1973; Julian, 1965). The function f is based on the theory of Roufosse and Klemens (1974) and accounts for saturation. It is given by

$$f(x) = \frac{2}{3}x^{-1/2} + \frac{1}{3}x \tag{S3}$$

for $x>1$ and is equal to unity for $x<1$. T_S is the temperature at which the phonon mean free path approaches the inter-atomic spacing

$$T_S = \frac{\sqrt{2}}{3\pi(6\pi^2)^{4/3}}\left(\frac{k_B}{\hbar}\right)^2 \frac{M\Omega^{2/3}\theta^2}{\gamma^2 k_B} \tag{S4}$$

We determine the values of the coefficients A=1.60 and B=0.91 by fitting to our first principles results and take values of all other parameters from a thermodynamic model (Stixrude and Lithgow-Bertelloni, 2011). For example, we find T_S = 960 K for $MgSiO_3$ perovskite at the density of the core-mantle boundary (5.29 gcm^{-3}) and a saturated value for the lattice thermal conductivity in the limit $T >> T_S$ of 5.7 $Wm^{-1}K^{-1}$. The isochoric heat capacity C accounts for the temperature dependence of phonon population at temperatures below the Debye temperature, and is important for comparing with experimental data near room temperature.

S2 Scaling Relation

To estimate the lattice thermal conductivity of $CaSiO_3$ perovskite, $FeSiO_3$ perovskite and FeO wüstite from our values for the magnesium end-members, we use the scaling derived from the Liebfreid-Schlömann relation

$$k_2 = k_1 \left(\frac{M_2}{M_1}\right)\left(\frac{v_2}{v_1}\right)^3 \left(\frac{\gamma_1}{\gamma_2}\right)^2 \left(\frac{\Omega_1}{\Omega_2}\right)^{2/3} \quad \text{(S5)}$$

where v is the Debye velocity, subscript 2 refers to the phase whose lattice thermal conductivity is being estimated and subscript 1 refers to a magnesium end-member: $MgSiO_3$ perovskite in the case of $CaSiO_3$ perovskite and $FeSiO_3$ perovskite and MgO periclase in the case of FeO wüstite. Values of all physical parameters were computed using a thermodynamic model (Stixrude and Lithgow-Bertelloni, 2011). For illustration, the values of k_2/k_1 obtained at core-mantle boundary conditions are: $CaSiO_3$ perovskite (1.02), $FeSiO_3$ perovskite (0.65), and FeO wüstite (0.41).

S3 Influence of Iron Impurities

The influence of iron impurities on lattice thermal conductivity is approximated using the theory of Klemens (1960) and Padture and Klemens (1997), which estimates the lattice

thermal conductivity of a binary solid solution as

$$k_S = k_V \left(\frac{\omega_S}{\omega_D}\right) \arctan\left(\frac{\omega_D}{\omega_S}\right) \quad \text{(S6)}$$

where ω_S is the phonon frequency where the mean free path is equal to that due to the solute atoms, ω_D the Debye frequency and k_V the lattice thermal conductivity of the solid solution in the absence of impurity scattering (i.e. the Voigt average of the two end-member values) given by

$$k_V = (1-x)k_1 + xk_2 \quad \text{(S7)}$$

where k_1 and k_2 are the lattice thermal conductivities of the component end-members, and x the mole fraction of component 2.

Based on Eq. (17) of Klemens (1960) and replacing the Debye frequency with the appropriate expression involving the Debye velocity and atomic volume we obtain

$$\left(\frac{\omega_S}{\omega_D}\right)^2 = \frac{k_B v}{(6\pi^2)^{1/3}\Omega^{2/3}\varepsilon k_V} \quad \text{(S8)}$$

where ε is related to the difference in the masses of the two component end-members M_1 and M_2

$$\varepsilon = \frac{(M_2 - M_1)^2}{\bar{M}^2} x(1-x) \quad \text{(S9)}$$

where $\bar{M}$ is the mean atomic mass of the solid solution. Substituting Eq. (S2) [LARS: Please check this the original Eq. S5 no longer exists] for k_V into (S8)

$$\left(\frac{\omega_S}{\omega_D}\right)^2 = \frac{\pi(6\pi^2)^{1/3}}{\sqrt{2}} \frac{k_B \gamma^2}{M v^2} \frac{T}{\varepsilon} \quad \text{(S10)}$$

where the second ratio on the right-hand side is related to T_S (S4 is no longer the same expression, so is this true? Yes.)

$$\left(\frac{\omega_S}{\omega_D}\right)^2 = \frac{1}{(6\pi^2)^{1/3}}\frac{T}{3\varepsilon T_S} \quad \text{(S11)}$$

Eqs. (S6) and (S11) show that the effect of scattering due to impurities increases with decreasing temperature, increasing mass difference and increasing impurity concentration. In the lower mantle impurity scattering is weak, because the temperature is high: $T >> T_S$ so that $\omega_S >> \omega_D$, $\arctan(\omega_D/\omega_S) \approx \omega_D/\omega_S$ and $k_S \approx k_V$ (Eq. (S6)). We note that, in his application, Klemens (1960) focused on the opposite, low-temperature, strong-scattering limit, for which $\arctan(\omega_D/\omega_S) = \pi/2$ and $k_S \propto T^{1/2}$, assuming $k_V \propto T^1$.

Taken together, Eqs. (S6), (S7) and (S11) can be used to estimate the lattice thermal conductivity of iron-bearing mineral phases. For example, using this method the lattice thermal conductivity of $(Mg_{0.94}Fe_{0.06})SiO_3$ perovskite is estimated to be 3 % less than that of the pure magnesium end-member. The effect of impurity scattering is somewhat larger for $(Mg_{0.8}Fe_{0.2})O$ ferropericlase, because of the larger mass difference and more concentrated solution. Its lattice thermal conductivity is found to be 21 % less than that of the pure magnesium end-member. We note that while our knowledge of the influence of impurities on thermal conductivity is still uncertain and requires further experiments, the model outlined here has been tested on similar systems including garnets (Padture and Klemens, 1997, Marquardt et al., 2009), and predicts a value for $(Mg_{0.8}Fe_{0.2})O$ at 2000 K and 14 GPa (7. W m^{-1} K^{-1}) that is identical to that of a more elaborate model that contains a free parameter fit to experimental data (Dalton et al., 2013).

S4 Heat-flux Analysis

The properties of the thermal boundary layer are related by (Jeanloz and Richter, 1979; Davaille and Jaupart, 1993)

$$Q = bk\left(\frac{\alpha g}{\kappa v}\right)^{1/3}\Delta T^{4/3} = \frac{k\Delta T}{\delta} \quad \text{(S12)}$$

where k is the thermal conductivity, α the thermal expansivity, g the gravitational acceleration, κ the thermal diffusivity, and v the kinematic viscosity, ΔT the temperature contrast across and δ the thickness of the thermal boundary layer. The coefficient b is empirically determined and equal to 0.1636. Thermodynamic properties at core-mantle boundary conditions were determined from a thermodynamic model (Stixrude and Lithgow-Bertelloni, 2011), while values for the kinematic viscosity were taken from recent first-principles calculations (Ammann et al., 2010).

Constraints on the temperature contrast across the core-mantle boundary are based on estimates of the mantle isentrope (derived from extrapolation of the mantle temperature from constraints at 660 km depth to the core-mantle boundary (Brown and Shankland, 1981; Stixrude and Lithgow-Bertelloni, 2011)) and the temperature at the top of the core (from knowledge of the melting point of iron alloys, and extrapolation from the inner core boundary to the core-mantle boundary (Brown and McQueen, 1986; Pozzo et al., 2012)).

Constraints on the heat-flux at the core-mantle boundary are based on: 1. The heat-flux carried by plumes and plume heads (3.5 TW) (Davies, 2007) and accounting for the increase in plume heat with depth due to the steeper isentrope in the plume (Stixrude and Lithgow-Bertelloni, 2011) and possible sub-adiabaticity in the background mantle (Schuberth et al., 2009), factors that may increase the heat-flux by a factor of three. This is a lower bound because mantle convection models show that not all the heat-flux from the core-mantle boundary is expressed as plumes (Lay et al., 2008). 2. The heat conducted down the core adiabat according to first principles calculations of the thermal conductivity and the adiabatic gradient of the outer core (de Koker et al., 2012; Pozzo et al., 2012). This is an upper bound because the top of the outer core may have a sub-adiabatic gradient (stably stratified).

References

Ammann, M.W., Brodholt, J.P., Wookey, J., Dobson, D.P., 2010. First-principles constraints on diffusion in lower-mantle minerals and a weak D" layer. Nature 465, 462–465.

Brown, J., McQueen, R., 1986. Phase-Transitions, Gruneisen-Parameter and Elasticity for Shocked Iron Between 77 GPa and 400 GPa. J. Geophys. Res. 91, 7485–7494.

Brown, J., Shankland, T., 1981. Thermodynamic Parameters in the Earth as Determined from Seismic Profiles. Geophys. J. R. astr. Soc. 66, 579–596.

Dalton, D.A., Wen-Pin, H., Hohensee, G.T., Cahill, D.G., Goncharov, A.F., 2013. Effect of mass disorder on the lattice thermal conductivity of MgO periclase under pressure. Sci. Rep., 3, 2400.

Davaille, A., Jaupart, C., 1993. Transient high-Rayleigh-number thermal-convection with large viscosity variations. J. Fluid Mech. 253, 141–166.

Davies, G.F., 2007. Mantle regulation of core cooling: A geodynamo without core radioactivity? Phys. Earth Planet. Inter. 160, 215–229.

de Koker, N., Steinle-Neumann, G., Vlcek, V., 2012. Electrical resistivity and thermal conductivity of liquid Fe alloys at high P and T, and heat flux in Earth's core. Proc. Natl. Acad. Sci. U. S. A. 109, 4070–4073.

Jeanloz, R., Richter, F., 1979. Convection, compoistion, and the thermal state of the lower mantle. J. Geophys. Res. 84, 5497–5504.

Julian, C., 1965. Theory of heat conduction in rare-gas crystals. Phys. Rev. 137, A128–A137.

Klemens, P., 1960. Thermal resistance due to point defects at high temperatures. Phys. Rev. 119, 507–509.

Lay, T., Hernlund, J., Buffett, B.A., 2008. Core-mantle boundary heat flow. Nat. Geosci. 1, 25–32.

Marquardt, H., Ganschow, S., Schilling, F.R., 2009a. Thermal diffusivity of natural and synthetic garnet solid solution series. Phys. Chem. Miner. 36, 107–118.

Padture, N.P., Klemens, P.G., 1997. Low thermal conductivity in garnets. J. Am. Ceram. Soc. 80, 1018–1020.

Pozzo, M., Davies, C., Gubbins, D., Alfe, D., 2012. Thermal and electrical conductivity of iron at Earth's core conditions. Nature 485, 355–358.

Roufosse, M., Klemens, P., 1973. Thermal-conductivity of complex dielectric crystals. Phys. Rev. B 7, 5379–5386.

Roufosse, M., Klemens, P., 1974. Lattice thermal-conductivity of minerals at high-tempeatures. J. Geophys. Res. 79, 703–705.

Schuberth, B.S.A., Bunge, H.-P., Ritsema, J., 2009. Tomographic filtering of high-resolution mantle circulation models: Can seismic heterogeneity be explained by temperature alone? Geochem. Geophys. Geosyst. 10.

Stixrude, L., Lithgow-Bertelloni, C., 2011. Thermodynamics of mantle minerals - II. Phase equilibria. Geophys. J. Int. 184, 1180–1213.

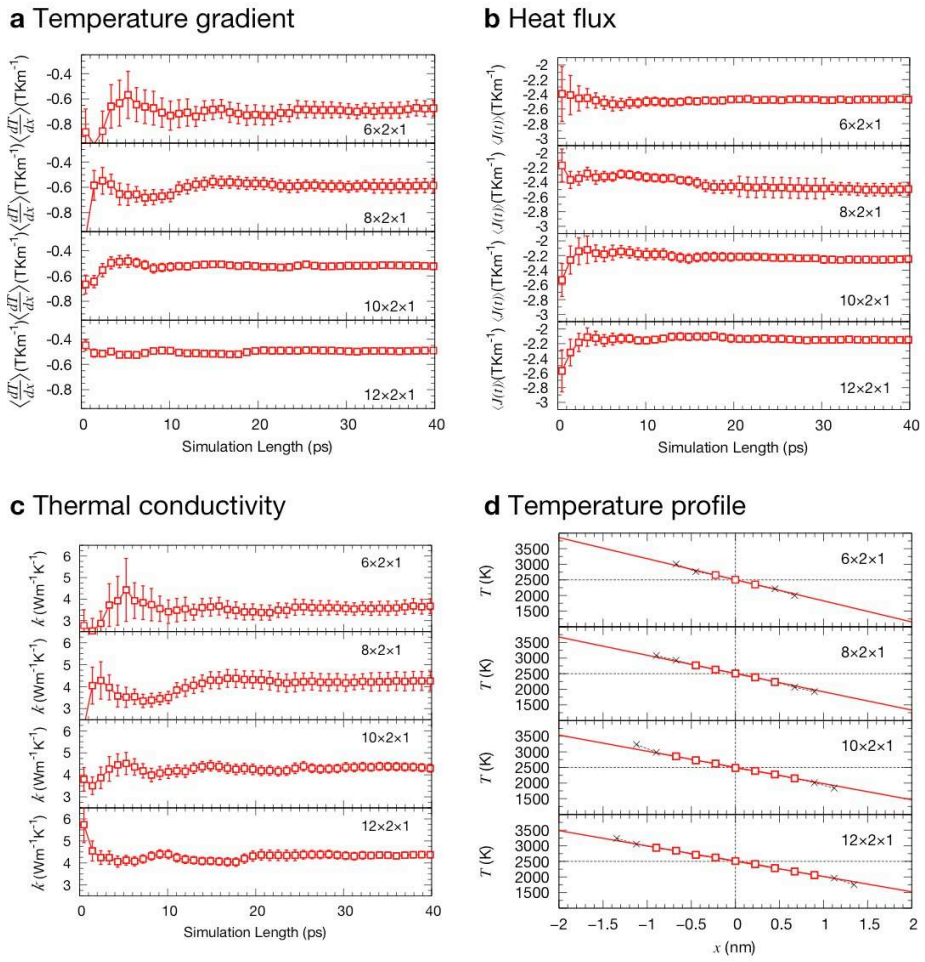

Fig. S1. Time average of the temperature gradient (a) heat-flux (b) and thermal conductivity (c), as a function of simulation length. Values are shown for calculations of the thermal conductivity in the [100] direction at 75 GPa and 2500 K. The first 10 ps of each simulation is allowed for equilibration. d, Corresponding temperature profiles for each simulation. The temperatures of the hot and cold sections (shown as an ×) are not included in the fit (solid line), used to estimate the temperature gradient. The labels refer to the dimensions of the simulations cells i.e. n×2×1 refers to a simulation cell with dimensions na×2b×c, where a, b and c are the unit cell parameters of perovskite.

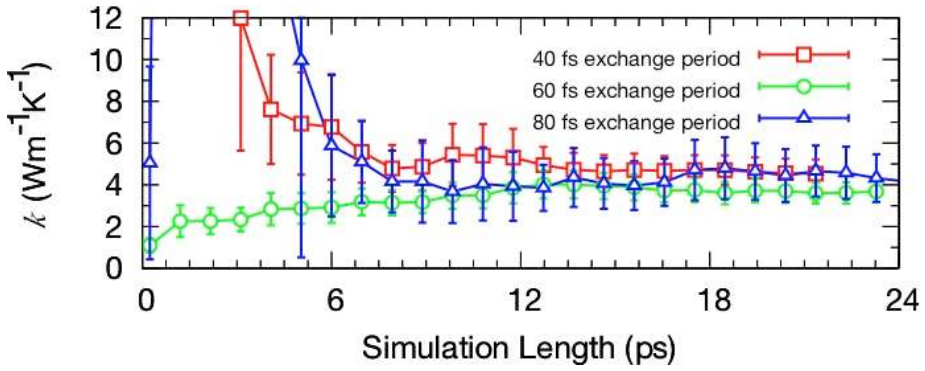

Fig. S2. Influence of exchange-frequency. Calculated thermal conductivity as a function of simulation length, for different exchange periods (40, 60 and 80 fs). Values are shown for the calculation of the thermal conductivity in the [100] direction, at 145 GPa and 4000 K, using a simulation cell with the dimensions $6a \times 2b \times c$, where a, b and c are the unit cell parameters of perovskite. All the simulations converge on the same value, irrespective of exchange period, indicating that Fourier's law is valid.

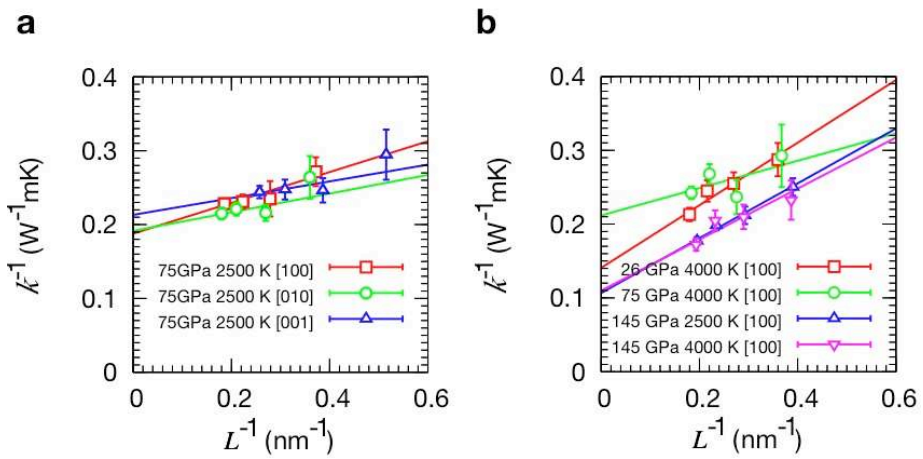

Fig. S3. Extrapolation to infinite simulation cell length. (a) At 75 GPa and 2500 K back extrapolation suggests that the thermal conductivity of $MgSiO_3$ perovskite is isotropic. (b) For all other temperature and pressure conditions studied the thermal conductivity was determined only in the [100] direction. Thermal conductivity is almost identical at 145 GPa and 2500 K and 145 GPa and 4000 K, suggesting saturation.

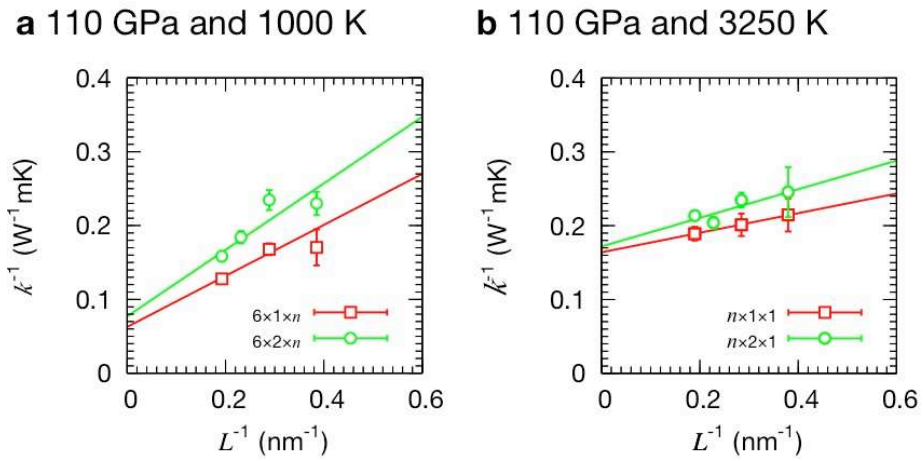

Fig. S4. Influence of cross-sectional area on calculated thermal conductivity. Doubling the cross-sectional perpendicular to the direction of the heat-flux appears to have only a minor influence on the estimated thermal conductivity values. The legends refer to the dimensions of the simulations cells i.e. n×m×1 refers to a simulation cell with dimensions na×mb×c, where a, b and c are the unit cell parameters of perovskite.

Table S1 Thermal conductivity (k) calculated by extrapolation to infinite simulation cell length and phonon mean free path (l) calculated from Equation 6, at each pressure and temperature condition. At 110 GPa and 1000 K and 110 GPa and 3250 K values are reported for simulation cells with different cross-sectional areas, giving an indication of finite-size effects.

P (GPa)	T (K)	Direction	Cross-Section	k ($Wm^{-1}K^{-1}$)	l (nm)
26	1000	[100]	$2b\times c$	7 ± 1.4	0.8 ± 0.3
75	2500	[100]	$2b\times c$	5.3 ± 0.7	0.3 ± 0.1
75	2500	[010]	$2a\times c$	5.2 ± 0.7	0.2 ± 0.2
75	2500	[001]	$2a\times 2b$	5.3 ± 0.7	0.2 ± 0.1
75	4000	[100]	$2b\times c$	4.7 ± 0.8	0.2 ± 0.2
110	1000	[100]	$b\times c$	16 ± 5	1.4 ± 0.6
110	1000	[100]	$2b\times c$	13 ± 3	1.5 ± 0.5
110	3250	[100]	$b\times c$	6 ± 1	0.2 ± 0.2
110	3250	[100]	$2b\times c$	5.8 ± 0.8	0.3 ± 0.2
145	2500	[100]	$2b\times c$	9 ± 1	0.9 ± 0.2
145	4000	[100]	$2b\times c$	9 ± 2	0.8 ± 0.4

Table S2 Time average of the temperature gradient ($\langle dT/dx \rangle$), heat-flux ($\langle \langle J(t) \rangle \rangle$) and thermal conductivity $\langle k \rangle$ for each simulation cell (x, y and z), at each pressure and temperature condition. t_{ex} is the time period between energy exchanges.

x (nm)	y (nm)	z (nm)	t_{ex} (fs)	$\langle dT/dx \rangle$ (TKm^{-1})	$\langle J(t) \rangle$ (TWm^{-2})	$\langle k \rangle$ (Wm^{-1}K^{-1})	*time* (ps)
26 GPa and 1000 K in the [100] direction							
2.779	0.960	0.665	80	0.148 ± 0.011	-0.515 ± 0.006	3.480 ± 0.273	112
3.706	0.960	0.665	80	0.127 ± 0.007	-0.498 ± 0.005	3.921 ± 0.232	134
4.632	0.960	0.665	80	0.119 ± 0.006	-0.487 ± 0.005	4.083 ± 0.243	85
5.559	0.960	0.665	80	0.102 ± 0.004	-0.480 ± 0.006	4.692 ± 0.199	97
75 GPa and 2500 K in the [100] direction							
2.690	0.934	0.647	40	0.676 ± 0.048	-2.490 ± 0.024	3.682 ± 0.265	68
3.586	0.934	0.647	40	0.586 ± 0.056	-2.493 ± 0.084	4.257 ± 0.433	50
4.483	0.934	0.647	40	0.519 ± 0.020	-2.247 ± 0.041	4.328 ± 0.181	51
5.379	0.934	0.647	40	0.490 ± 0.013	-2.148 ± 0.026	4.380 ± 0.131	51
75 GPa and 2500 K in the [010] direction							
0.897	2.800	0.647	40	0.679 ± 0.074	-2.569 ± 0.036	3.786 ± 0.417	50
0.897	3.734	0.647	40	0.531 ± 0.025	-2.454 ± 0.036	4.623 ± 0.229	56
0.897	4.668	0.647	40	0.511 ± 0.017	-2.381 ± 0.031	4.657 ± 0.174	54
0.897	5.601	0.647	40	0.475 ± 0.015	-2.213 ± 0.045	4.659 ± 0.175	50
75 GPa and 2500 K in the [001] direction							
0.897	0.934	1.941	40	0.578 ± 0.066	-1.963 ± 0.027	3.393 ± 0.390	114
0.897	0.934	2.588	40	0.487 ± 0.032	-1.976 ± 0.021	4.058 ± 0.272	53
0.897	0.934	3.235	40	0.469 ± 0.025	-1.894 ± 0.022	4.042 ± 0.220	52
0.897	0.934	3.882	40	0.452 ± 0.013	-1.854 ± 0.036	4.099 ± 0.141	50
75 GPa and 4000 K in the [100] direction							
2.722	0.937	0.653	80	0.645 ± 0.092	-2.206 ± 0.049	3.419 ± 0.495	73
3.630	0.937	0.653	80	0.514 ± 0.048	-2.173 ± 0.060	4.226 ± 0.414	53
4.538	0.937	0.653	80	0.548 ± 0.025	-2.044 ± 0.043	3.732 ± 0.186	58
5.445	0.937	0.653	80	0.483 ± 0.015	-1.991 ± 0.034	4.124 ± 0.145	88
110 GPa and 1000 K in the [100] direction							
2.596	0.458	0.628	80	0.159 ± 0.025	-0.903 ± 0.013	5.666 ± 0.886	132
2.596	0.458	0.628	80	0.149 ± 0.028	-0.905 ± 0.013	6.079 ± 1.162	72
3.461	0.458	0.628	80	0.138 ± 0.009	-0.866 ± 0.010	6.259 ± 0.394	189
3.461	0.458	0.628	80	0.151 ± 0.010	-0.853 ± 0.014	5.655 ± 0.399	83
5.191	0.458	0.628	80	0.115 ± 0.004	-0.819 ± 0.009	7.126 ± 0.275	141
5.191	0.458	0.628	80	0.100 ± 0.007	-0.854 ± 0.029	8.528 ± 0.675	37
2.596	0.916	0.628	80	0.148 ± 0.016	-0.580 ± 0.006	3.926 ± 0.423	181
2.596	0.916	0.628	80	0.121 ± 0.024	-0.577 ± 0.010	4.768 ± 0.958	116
3.461	0.916	0.628	80	0.134 ± 0.007	-0.573 ± 0.011	4.264 ± 0.247	108
4.326	0.916	0.628	80	0.103 ± 0.005	-0.565 ± 0.009	5.428 ± 0.251	117
5.191	0.916	0.628	80	0.100 ± 0.004	-0.555 ± 0.011	5.549 ± 0.257	109
5.191	0.916	0.628	80	0.078 ± 0.005	-0.551 ± 0.008	7.079 ± 0.498	73
110 GPa and 3250 K in the [100] direction							
2.636	0.459	0.635	60	0.774 ± 0.080	-3.605 ± 0.059	4.659 ± 0.488	108
3.514	0.459	0.635	60	0.694 ± 0.047	-3.448 ± 0.108	4.969 ± 0.376	53
5.271	0.459	0.635	60	0.594 ± 0.026	-3.138 ± 0.070	5.286 ± 0.260	50
2.636	0.919	0.635	60	0.595 ± 0.081	-2.424 ± 0.046	4.073 ± 0.562	50
3.514	0.919	0.635	60	0.547 ± 0.023	-2.331 ± 0.022	4.263 ± 0.180	142
4.393	0.919	0.635	60	0.462 ± 0.016	-2.267 ± 0.037	4.901 ± 0.188	78
5.271	0.919	0.635	60	0.456 ± 0.013	-2.135 ± 0.033	4.686 ± 0.152	65
145 GPa and 2500 K in the [100] direction							
2.562	0.907	0.622	40	0.674 ± 0.031	-2.692 ± 0.023	3.997 ± 0.189	110
3.416	0.907	0.622	40	0.541 ± 0.029	-2.551 ± 0.031	4.718 ± 0.264	74
4.270	0.907	0.622	40	0.491 ± 0.015	-2.475 ± 0.026	5.043 ± 0.167	58
5.124	0.907	0.622	40	0.423 ± 0.031	-2.389 ± 0.025	5.644 ± 0.163	62
145 GPa and 4000 K in the [100] direction							
2.586	0.909	0.626	80	0.548 ± 0.063	-2.355 ± 0.021	4.301 ± 0.493	137
3.448	0.909	0.626	80	0.493 ± 0.038	-2.349 ± 0.033	4.765 ± 0.375	56
4.310	0.909	0.626	80	0.457 ± 0.030	-2.228 ± 0.023	4.879 ± 0.325	104
5.172	0.909	0.626	80	0.391 ± 0.018	-2.271 ± 0.040	5.805 ± 0.282	52